catalysts

MDPI

Article

F,O,S-Codoped Graphitic Carbon Nitride as an Efficient Photocatalyst for the Synthesis of Benzoxazoles and Benzimidazoles

Alberto Santiago-Aliste [1], Eva Sánchez-Hernández [1], Celia Andrés-Juan [2], Pedro Chamorro-Posada [3], Guillermo Antorrena [4], Jesús Martín-Gil [1] and Pablo Martín-Ramos [1,*]

[1] Department of Agricultural and Forestry Engineering, ETSIIAA, Universidad de Valladolid, Avenida de Madrid 44, 34004 Palencia, Spain
[2] GIR Asymmetric Synthesis, Universidad de Valladolid, Campus Miguel Delibes, Paseo Belén 7, 47011 Valladolid, Spain
[3] Department of Theory of Signal and Communications and Telematic Engineering, ETSIT, Universidad de Valladolid, Paseo de Belén 15, 47011 Valladolid, Spain
[4] Laboratorio de Microscopias Avanzadas (LMA), Edificio I+D, Campus Río Ebro, Universidad de Zaragoza, C/Mariano Esquillor s/n, 50018 Zaragoza, Spain
* Correspondence: pmr@uva.es

Abstract: Graphitic carbon nitride (g-C_3N_4) is a metal-free heterogeneous catalyst that has attracted attention because of its good chemical stability, cost-effectiveness, and environmental friendliness. In the work presented herein, F,O,S-codoped carbon nitride was synthesized by heating a mixture of melamine cyanurate and trifluoromethanesulfonic acid at 550 °C for 50 min. The obtained product was characterized by transmission electron microscopy, infrared spectroscopy, X-ray powder diffraction, CHNS elemental analysis, total combustion-ion chromatography, X-ray photoelectron spectroscopy, scanning electron microscopy coupled with energy-dispersive X-ray spectroscopy, and UV-Vis spectroscopy. Results point to an F,O,S-codoped g-C_3N_4. The material was applied as a photocatalyst for the formation of benzoxazoles and benzimidazoles by condensation–aromatization of 2-aminophenol or 1,2-phenylenediamine with suitable aldehydes (viz. benzaldehyde, 4-chlorobenzaldehyde, 2-naphthaldehyde, 2-hydroxybenzaldehyde, and 2-methoxybenzaldehyde), obtaining yields of up to 90% in 15 min under visible light irradiation, with good selectivity and reusability. Thus, the reported findings suggest that this F,O,S-codoped g-C_3N_4 may hold promise as a metal-free photocatalyst for the rapid synthesis of 2-arylbenzoxazoles and 2-arylbenzimidazoles.

Keywords: photocatalytic synthesis; doped g-C_3N_4; 2-arylbenzoxazoles; 2-arylbenzimidazoles

Citation: Santiago-Aliste, A.; Sánchez-Hernández, E.; Andrés-Juan, C.; Chamorro-Posada, P.; Antorrena, G.; Martín-Gil, J.; Martín-Ramos, P. F,O,S-Codoped Graphitic Carbon Nitride as an Efficient Photocatalyst for the Synthesis of Benzoxazoles and Benzimidazoles. *Catalysts* **2023**, *13*, 385. https://doi.org/10.3390/catal13020385

Academic Editors: Orhan Şişman, Surjyakanta Rana, José Joaquín Velázquez García and Rajesh Dagupati

Received: 30 December 2022
Revised: 4 February 2023
Accepted: 8 February 2023
Published: 10 February 2023

1. Introduction

Aryl-substituted benzoxazoles and benzimidazoles are a valuable class of heterocyclic compounds that have a wide range of biological activities, including anti-inflammatory [1], antimicrobial [2], antitumor [3], antiviral, antihypertensive, and antihistaminic activities [4].

A well-known method for the preparation of such benzoxazoles and benzimidazoles is the condensation–aromatization of 2-aminophenol and 2-phenylenediamine, respectively, with aldehydes using Brønsted-Lowry acid catalysts [5]. Among the potential catalysts for this reaction process, the ones that have received the most attention have been the task-specific ionic liquids [6], the Brønsted acidic ionic liquid gels [5], and the [CholineCl][oxalic acid] deep eutectic solvent (DES) [7].

An alternative for photocatalyst-mediated organic reactions may be the use of graphitic carbon nitride (g-C_3N_4). This heterogeneous catalyst has attracted attention because of its good chemical stability, cost-effectiveness, and eco-friendliness. As summarized in the

recent review paper by Verma et al. [8], g-C_3N_4 has been successfully used in visible-light-promoted oxidation of alcohols; synthesis of sulfoxides, phenols, and esters; reduction of nitro compounds; carbonyl compounds formation; and coupling/cross-reactions. Different strategies for enhancing g-C_3N_4 photocatalysis for visible-light-driven organic transformation have been put forward, including combination with molecular photocatalysts and transition metal catalysts or organocatalysts, doping with different elements, or the formation of heterojunctions with inorganic photocatalysts [9].

If g-C_3N_4 is intended to be used as a Brønsted-Lowry acid catalyst, acidification and multielement doping may be regarded as promising approaches, supported by the previously reported successful synthesis of, for instance, sulfuric acid-modified g-C_3N_4 [10]; sulfonated mesoporous g-C_3N_4 (mpg-C_3N_4/SO_3H) [11,12]; and P,S,O-codoped g-C_3N_4 [13].

In this paper, in line with the above-discussed multielement doping strategy, we report a new catalyst based on the F,O,S-codoping of g-C_3N_4, designed to combine the advantages of S- and O-doping with those resulting from F-doping, facilitating the charge separation across the heptazine rings and attracting photoexcited electrons.

2. Results

2.1. Characterization of the Photocatalyst

According to scanning electron microscopy (SEM) micrographs (Figure 1), the material prepared by pyrolysis showed a crumpled morphology, generally associated with a turbostratic staking type [14].

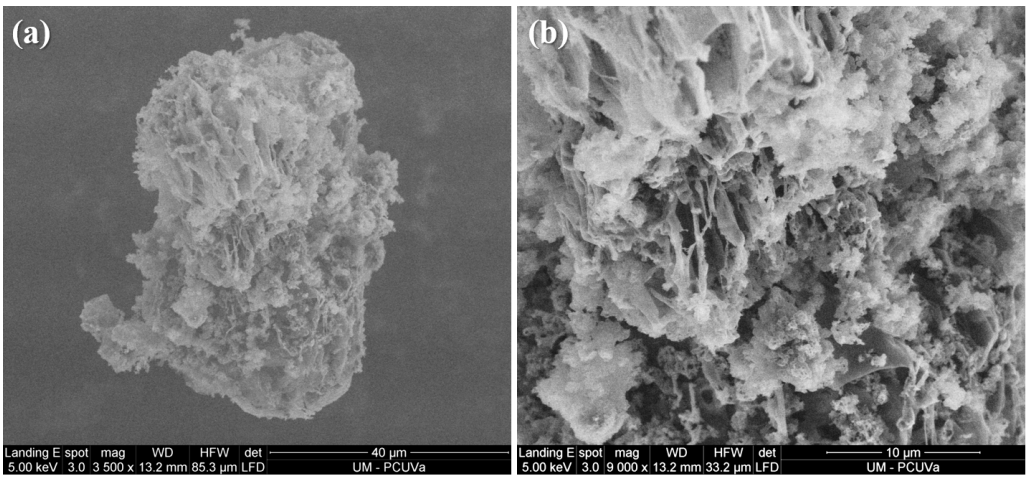

Figure 1. Scanning electron microscopy micrographs of F,O,S-codoped g-C_3N_4 showing a crumped morphotype at (**a**) 3500× and (**b**) 9000× magnification.

Transmission electron microscopy (TEM) images of the obtained product are shown in Figure 2a. These micrographs are similar to those obtained by Jiang et al. [15] for S-doped g-C_3N_4 (Figure 2b) and, at higher magnification (Figure 2c), show the expected interlayer distance for turbostratic-like carbon nitride, i.e., 0.33 nm.

The infrared spectrum of the F,O,S-codoped g-C_3N_4 showed bands at 3249, 3157, 3084, 2982, 1627 (C=O), 1566 (C=N), 1534, 1453, 1392, 1312 (C–N), 1277, 1225 (C–NH–C), 1131, 1027, 890, 804 (tri-*s*-triazine units), 639, and 495 cm^{-1} (Figure S1), indicating the good preservation of the basic heptazine structure and the introduction of F, S, and O atoms (from the decomposition of triflic acid) in the g-C_3N_4 structure, replacing N atoms [13,16]. The shoulder at 1082 cm^{-1}, attributable either to C–F bonds [17] or to C–S/C–O bonds [18] would support the F-, S-, and O-doping. Other bands presumably related to C–F bonds are those at 639 cm^{-1} (a wagging mode) and 1027 cm^{-1} (ascribed to *semi-ionic* C-F_{II} bonds [19], although it may also be assigned to C–O stretching). The band at 1277–1263 cm^{-1} may be ascribed to a C–F vibration mode, although it may be overlapped with C–O or C–N modes.

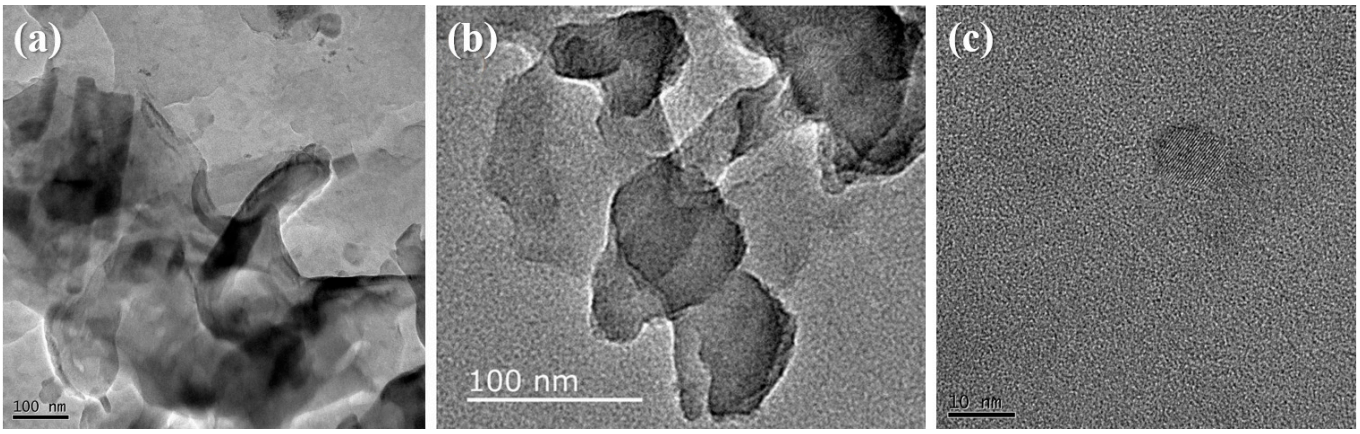

Figure 2. Comparison of transmission electron microscopy images of (**a**) F,O,S-codoped g-C_3N_4 and (**b**) S-doped g-C_3N_4 (reproduced from [15] under CC 4.0 license); (**c**) view of an agglomerate of 30 nanosheets of F,O,S-codoped g-C_3N_4 with an interlayer distance of 0.33 nm.

X-ray powder diffraction (XRPD) was used for the characterization of the main phase composition of the obtained product. The XRPD pattern showed the main (002) peak at $2\theta = 27.636^\circ$ (Figure S2), characteristic of an interlayer stacking of conjugated aromatic systems. This high-angle peak corresponds to an average interlayer distance d = 0.323 nm, consistent with that determined from TEM micrographs and with the (002) plane of graphitic carbon nitride and slightly shorter than the one usually reported for pristine g-C_3N_4 (d = 0.325 nm). This narrower layer spacing, usually interpreted as a planarization of undulated carbon nitride layers, could be a result of the acidification and the heat treatment during the synthesis, but may also be the result of doping [20]. As regards the low-angle region, associated with the in-plane ordering of tri-*s*-triazine units, the peak observed at $2\theta = 12.83^\circ$ is the one expected for the (100) plane in pristine g-C_3N_4 (i.e., a calculated distance of 0.69 nm, corresponding to the hole-to-hole distance of nitride pores [21]), suggesting that the doping did not result in noticeable shortening/lengthening of the in-plane repeated motif distance.

CHNS elemental analysis results (Table S1) indicated a bulk composition with carbon, hydrogen, nitrogen, sulfur, and oxygen+fluorine contents of 27.4 ± 0.1%, 2.2 ± 0.2%, 41.2 ± 0.1%, 1.1 ± 0.1%, and 28.1 ± 0.5%, respectively. The total fluorine content obtained by combustion-ion chromatography (C-IC) was 14 ± 1%. Hence, fluorine and oxygen doping would outweigh sulfur doping.

The surface chemistry of the doped g-C_3N_4 was investigated by X-ray photoelectron spectroscopy (XPS). The wide-scan XPS spectrum is shown in Figure 3. According to the elemental quantification (Table 1), the obtained C/N ratio was 0.87, close to that expected for g-C_3N_4, albeit with a slight excess of carbon (tentatively ascribed to a contribution of adventitious carbon and/or carbon from triflic acid).

When XPS high-resolution regions (Figure 4) were used for analyses, the C 1s region presented the main maximum at 288.1 eV, which is in agreement with the values described in the literature for the carbon environment in the typical heptazine structure of g-C_3N_4 (and which are similar to those expected for melamine). Ideally, in the heptazine structure of g-C_3N_4, unique carbon environment in the structure but, in this case, this main signal was one should see a single carbon signal corresponding to the accompanied by a series of shoulders. One appeared on the low binding energy side, consistent with the presence of adventitious carbon, and others—corresponding to more oxidized environments of carbon—would support the presence of fluorine in the sample and would be consistent with carbon from triflic origin. The N 1s region presented a maximum at 398.6 eV, in agreement with the binding energy described in the literature for the sp^2 nitrogen environment, but accompanied by another signal at 400.2 eV, consistent with that described for the tertiary or bridging nitrogens of the g-C_3N_4 structure. Similar environments corresponding to amino

terminals are also close to this energy. The sp^2/sp^3 ratio of nitrogen environments expected for the g-C_3N_4 structure should be in a 6-to-2 relationship (i.e., 75/25), but the value obtained in the fit pointed to a lower N sp^2 signal, resulting in an sp^2/sp^3 ratio of 56/44. This finding would further support the presence of fluorine, given that a transformed hybridization mode from sp^2 to sp^3 has been reported for fluorinated g-C_3N_4 [22].

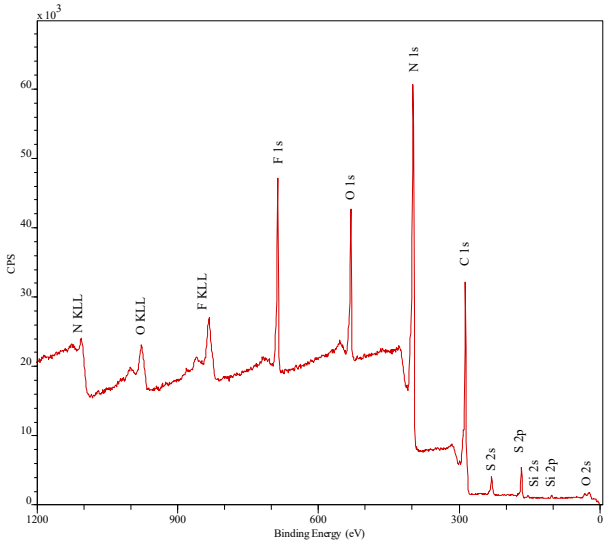

Figure 3. X-ray photoelectron spectroscopy (wide scans) spectrum for F,O,S-codoped g-C_3N_4.

Table 1. X-ray photoelectron spectroscopy results, in atomic percentage, for F,O,S-codoped g-C_3N_4.

	C 1s %at.	N 1s %at.	F 1s %at.	O 1s %at.	S 2p %at.	Si 2p %at.
Wide scans	36.24	41.81	9.73	9.67	2.23	0.32
High-resolution regions	37.07	42.69	9.05	8.99	1.93	0.27

An additional study by energy-dispersive X-ray spectroscopy (EDS) (Figures S3 and S4) aimed at obtaining complementary information on the elemental composition was also carried out. The elemental mapping (Figure S4) showed a homogeneous distribution of the doping elements in the photocatalyst. The elemental composition obtained by EDS (Table 2) was relatively coincident with those obtained by multi-elemental analysis and XPS, although it showed higher carbon and sulfur contents and a lower fluorine percentage. The differences observed may be related to the microheterogeneity of the sample, with different remaining contents of triflic acid (not decomposed in the thermal process) and of sulfur fluoride oxides ($F_{10}OS_2$, F_4OS, SO_2F_2) formed from CF_3SO_3H. The presence of the doping elements (viz. F, S, and O) in the g-C_3N_4 framework would thus be variable (depending also on the characterization technique) but sufficient to produce electronic structure modifications and subsequent changes in the bandgap. Thus, it is expected that the substitution of S for lattice N displays an increased valence bandwidth, an elevated conduction band minimum, and a slightly reduced absorbance, such that the photoreactivity results are higher than those of pristine g-C_3N_4 under visible light irradiation [23]. Furthermore, F-functionalization or F-doping also appears to be promising for visible-light photocatalysis applications [24]. On the other hand, as regards possible C-doping from the degradation of triflic acid, Dong et al. [25] demonstrated that C self-doping could induce intrinsic electronic and band structure changes in g-C_3N_4 via the formation of delocalized big π bonds to increase visible light absorption.

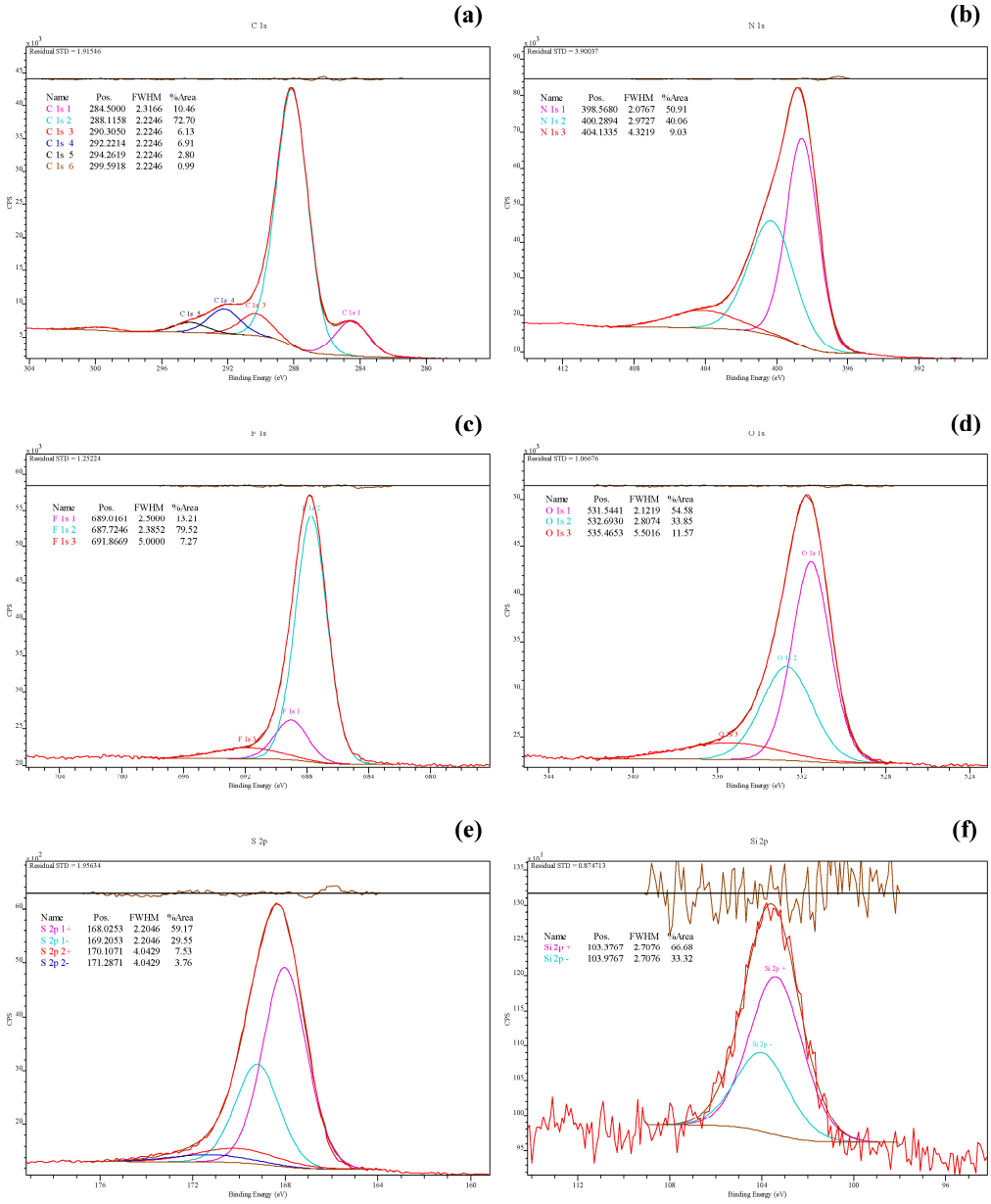

Figure 4. X-ray photoelectron spectroscopy (high-resolution regions) spectra of F,O,S-codoped g-C_3N_4: (**a**) C 1s, (**b**) N 1s, (**c**) F 1s, (**d**) O 1s, (**e**) S 2p, (**f**) Si 2p. The regions have been calibrated by taking C 1s C–C at 284.5 eV as an energy calibration reference.

Table 2. Energy-dispersive X-ray spectroscopy analysis results of F,O,S-codoped g-C_3N_4.

C %at.	N %at.	F %at.	O %at.	S %at.	Si %at.
52.58	37.10	1.40	2.48	4.26	2.18

Concerning the aforementioned changes in the bandgap as a result of doping, Figure 5 displays the UV-Vis absorption spectrum of F,O,S-codoped g-C_3N_4. The absorbance was obtained from the diffuse reflectance of the sample (R) using the Kubelka–Munk function $F(R) = (1 - R)^2/(2R)$. The bandgap calculated from these results using the Tauc plot method was Eg = 3.08 eV, higher than that of pristine g-C_3N_4 (2.7 eV). As noted by Sun, Li and Feng [22], the enlarged bandgap suffers from the shortcoming of light absorption, although the optical absorption tail in the longer wavelength implies the generation of a defect state or heteroatom level.

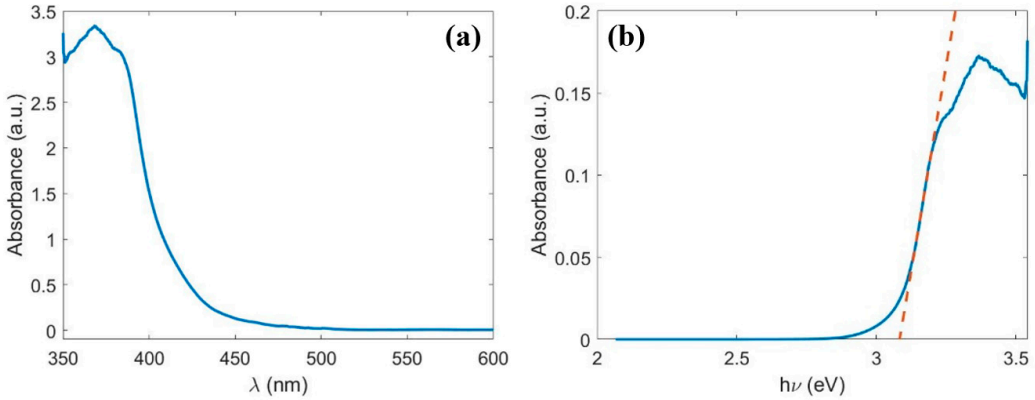

Figure 5. (**a**) UV–visible absorbance of F,O,S-codoped g-C_3N_4 in terms of Kubelka–Munk absorbance units, and (**b**) Tauc plot.

Figure S5 displays the emission spectra of F,O,S-codoped g-C_3N_4 and pristine g-C_3N_4 (prepared only from melamine cyanurate) under 365 nm excitation. Even though both spectra exhibited similar features, some differences could be observed. Compared to the luminescence produced by the reference material (pristine g-C_3N_4), that of the F,O,S-codoped g-C_3N_4 displayed a slight red shift of the emission peak. At the same time, an important reduction of the maximum emission and a spectral broadening in the luminescence of the sample could be observed. The shift toward longer wavelengths points to the presence of sub-gap defects in the material, while the lower emission intensity may be attributed to increasing non-radiative recombination rates and the shorter lifetime of the carriers [26].

2.2. Photocatalytic Synthesis of Benzoxazoles and Benzimidazoles

2.2.1. Catalytic Conditions and Yields

The chemical structures of the main products of photocatalytic synthesis are shown in Figure 6.

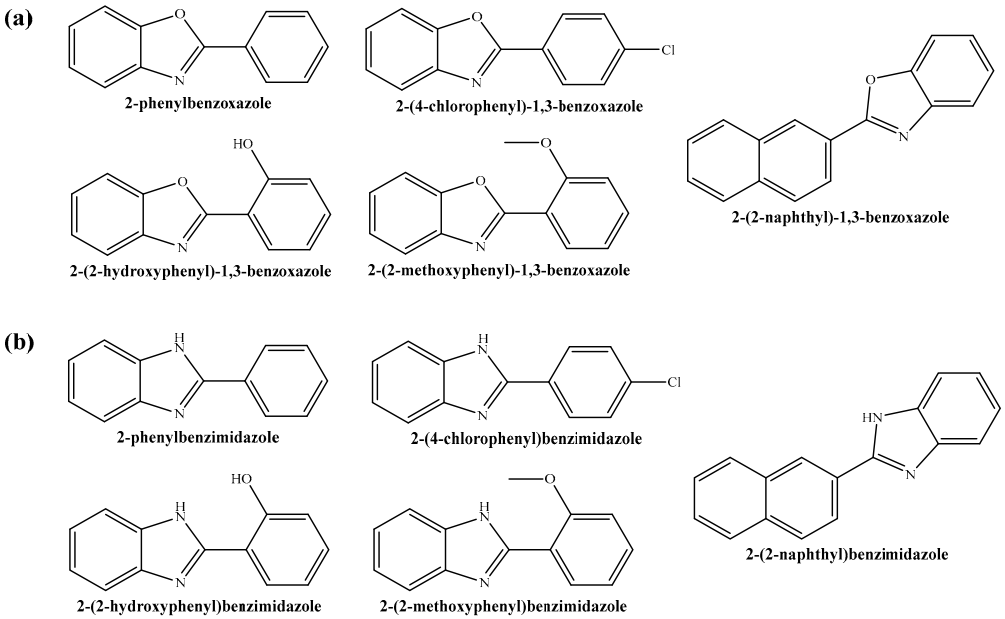

Figure 6. Synthesized products: (**a**) benzoxazoles and (**b**) benzimidazoles.

Detailed conditions of the photocatalytic synthesis of the benzoxazoles and benzimidazoles are summarized in Tables 3 and 4, respectively.

Table 3. Photocatalytic conditions for the synthesis of benzoxazoles using F,O,S-codoped g-C_3N_4 vs. pristine g-C_3N_4 (labeled with an asterisk).

	Aldehyde		2-Aminophenol		Catalyst		Irrad. Time (min)	Total Weigh (mg)	Benzoxazole (mg)	TON [a]	TOF [b] (h^{-1})	Yield [c] (%)
	mg	mmol	mg	mmol	mg	wt%						
Benzaldehyde	228	2.15	225	2.06	3	0.65	15	456	58	9	36	12.7
	301	2.84	299	2.73	3	0.50	15	603	33	5	21	5.5
	280	2.64	274	2.51	6	1.07	30	560	490	39	77	87.5
	53	0.50	55	0.52	1	0.92	30	109	60	28	56	55.0
	53	0.50	53	0.49	0.5	0.47	15	107	30	31	123	28.0
	53	0.50	55	0.52	1.0 *	0.92 *	30	109	25	12	23	22.9
4-chlorobenzaldehyde	399	2.84	299	2.74	3	0.43	30	701	40	5	11	5.7
	389	2.77	302	2.77	10	1.43	30	701	600	24	48	85.6
	415	2.95	322	2.95	9	1.20	30	746	605	27	54	81.1
	70	0.50	55	0.50	1.3	1.03	15	126	60	19	74	47.6
	70	0.50	55	0.50	0.6	0.48	15	126	30	20	80	23.8
	70	0.50	55	0.50	1.3 *	1.03 *	15	126	15	5	18	11.9
2-naphtaldehyde	78	0.50	55	0.50	2.6	1.91	30	136	80	12	23	58.8
	78	0.50	55	0.50	2.6	1.91	30	136	90	13	26	66.2
	156	1.00	110	1.00	3.0	1.11	30	269	180	23	46	66.9
	156	1.00	110	1.00	2.0	0.75	15	268	100	20	82	37.3
	156	1.00	110	1.00	4.0	1.48	15	270	150	14	57	55.5
	156	1.00	110	1.00	2.0 *	0.75 *	15	268	35	7	29	13.1
2-hydroxybenzaldehyde	61	0.50	55	0.50	1.2	1.02	15	117	92	34	134	78.6
	61	0.50	55	0.50	1.2	1.02	15	117	88	32	128	75.2
	122	1.00	110	1.00	1.8	0.77	15	234	120	29	116	51.3
	122	1.00	110	1.00	3.0	1.28	30	235	185	27	53	78.7
	122	1.00	110	1.00	4.5	1.90	30	237	196	19	38	82.7
	122	1.00	110	1.00	3.0 *	1.28 *	30	235	45	7	13	19.1
2-methoxybenzaldehyde	68	0.50	55	0.50	1.2	0.97	15	124	65	22	88	52.4
	68	0.50	55	0.50	1.2	0.97	15	124	72	10	40	58.1
	136	1.00	110	1.00	3.0	1.20	15	249	150	20	80	60.2
	136	1.00	110	1.00	5.0	2.00	30	250	189	16	32	75.6
	136	1.00	110	1.00	6.0	2.34	30	251	195	13	26	77.7
	136	1.00	110	1.00	3.0 *	1.2 *	30	249	34	5	19	13.7

[a] TON = moles of product formed per mole of catalyst. [b] TOF = TON/time (h). [c] Yield: Isolated yield after column chromatography. * pristine g-C_3N_4.

Table 4. Photocatalytic conditions for the synthesis of benzimidazoles using F,O,S-codoped g-C_3N_4 vs. pristine g-C_3N_4 (indicated with an asterisk).

	Aldehyde		1,2-Phenylenediamine		Catalyst		Irrad. Time (min)	Total Weight (mg)	Benzimidazole (mg)	TON [a]	TOF [b] (h^{-1})	Yield [c] (%)
	mg	mmoL	mg	mmoL	mg	wt%						
Benzaldehyde	106	1.00	108	1.00	6.0	2.73	30	220	143	4	8	65
	212	2.00	216	2.00	3.2	0.74	30	431	78	2	4	18
	280	2.64	274	2.53	6.0	1.09	30	550	347	4	8	63
	53	0.50	55	0.52	1.0	0.92	15	109	49	18	72	45
	53	0.50	53	0.49	0.5	0.47	15	107	26	21	84	24
	53	0.50	55	0.52	1.0 *	0.92 *	15	109	16	6	24	15
4-chlorobenzaldehyde	140	1.00	108	1.00	3.0	1.20	30	251	189	38	76	75
	280	2.00	216	2.00	10.0	2.04	30	490	382	15	31	78
	415	3.91	433	4.00	9.0	1.05	30	857	686	31	61	80
	70	0.50	55	0.50	1.3	1.03	15	126	98	31	122	78
	70	0.50	55	0.50	0.6	0.48	15	126	32	21	84	25
	70	0.50	55	0.50	1.3 *	1.0 *	15	126	15	5	19	12
2-naphtaldehyde	78	0.50	55	0.50	2.6	1.91	15	136	106	15	62	78
	156	1.00	108	1.00	0.9	0.34	15	265	48	20	78	18
	312	2.00	216	2.00	1.3	0.25	15	529	132	38	154	25
	78	0.50	55	0.50	2.0	1.50	30	135	115	67	134	85
	78	0.50	55	0.50	4.0	2.92	30	137	112	11	21	82
	78	0.50	55	0.50	2.0 *	1.5 *	30	135	30	17	35	22
2-hydroxybenzaldehyde	122	1.00	108	1.00	1.4	0.61	15	231	74	24	94	32
	244	2.00	216	2.00	2.7	0.58	15	462	116	19	76	25
	61	0.50	108	0.50	2.3	1.35	15	171	152	29	116	89
	61	0.50	108	0.50	2.7	1.57	30	172	143	24	95	83
	61	0.50	108	0.50	4.0	2.31	30	173	151	17	67	87
	61	0.50	108	0.50	4.0 *	2.3 *	30	173	33	17	67	19
2-methoxybenzaldehyde	136	1.00	108	1.00	2.2	0.89	15	246	81	33	132	43
	312	2.00	216	2.00	1.9	0.77	15	246	86	18	73	35
	68	0.50	54	0.50	2.2	1.77	15	124	94	38	152	76
	68	0.50	54	0.50	2.5	2.02	30	124	87	18	35	70
	68	0.50	54	0.50	1.9	0.85	30	124	83	18	36	67
	68	0.50	54	0.50	2.5 *	2.0 *	30	124	15	18	35	12

[a] TON = moles of product formed per mole of catalyst. [b] TOF = TON/time (h). [c] Yield: Isolated yield after column chromatography. * pristine g-C_3N_4.

In the absence of irradiation, the reactions did not progress, regardless of the amount of photocatalyst used.

With irradiation times of 15–30 min, when the amount of photocatalyst ranged from 0.25 to 1.02 wt%, the yields of the desired product formed ranged from 5.5 to 58.1% in the case of benzoxazoles and from 18 to 67% in the case of benzimidazoles. However, upon the increase of the amount of photocatalyst used, with contents between 1.02 and 2.34 wt%, the desired product yields increased, with values in the 75.2–87.5% and 75.0–89% intervals for benzoxazoles and benzimidazoles, respectively. These yields were similar to those previously reported for metallic catalysts (between 70 and 95%, at a working temperature of 80 °C) in the case of the synthesis of 2-phenylbenzoxazole [27].

The influence of the doping on the yield was assessed by comparison with the yields obtained using pristine g-C_3N_4 (0.75–2.31 wt%): whereas yields of up to 90% were reached with F,O,S-codoped g-C_3N_4, those obtained with pristine g-C_3N_4 remained below 23%.

A closer examination of the reaction yields led us to observe that they were also dependent on the substituents present on the substrates (having electron-withdrawing/donating groups) and on steric factors, but without substantial differences. The highest yield in the formation of benzimidazoles (89% yield, TOF 116 h^{-1}) was obtained for the hydroxylated derivative of benzaldehyde, while the best yield for benzoxazoles (87.5%, TOF 77 h^{-1}) was obtained for the same benzaldehyde without any substituent.

Concerning the effect of temperature on the reactions under consideration, it is worth noting that it was very important, given that, when temperatures above 40 °C were reached, the yield of the formation of benzoxazoles and benzimidazoles was reduced in favor of unwanted red-colored species.

With regard to the selectivity, it was determined for the two final products for which the best yields were attained and their intermediates, using HRMS-ESI (Figure S6). The product ratio of the (*E*)-2-(benzylideneamino)phenol (*m*/*z* 196.08 $[M + H]^+$) intermediate to the 2-phenylbenzo[d]oxazole (*m*/*z* 194.06 $[M+H]^+$) desired product was 12/88, while that of the (*E*)-2-(((2-aminophenyl)imino)methyl)phenol (*m*/*z* 211.09 $[M + H]^+$) intermediate to the 2-(2-hydroxyphenyl)benzimidazole (*m*/*z* 209.07 $[M + H]^+$) desired product was 7/93, lower than those reported for [CholineCl][Oxalic Acid] catalyzed synthesis [7], for which selectivities of up to 1/99 were attained in the case of some benzoxazoles.

Regarding the reusability of F,O,S-codoped g-C_3N_4, shown in Figure 7 for the aforementioned two compounds for which the highest yields were obtained, four recycle runs without significant loss of its catalytic activity were confirmed. Throughout these runs, the structural characteristics remained unaltered, but a change was observed in the FTIR spectra (Figure S7): a decrease in the intensity of the bands at 639 and 1027 cm^{-1} (attributed to C-F and C-O vibrations), suggesting some role of fluorine and oxygen active sites/species in the catalytic behavior.

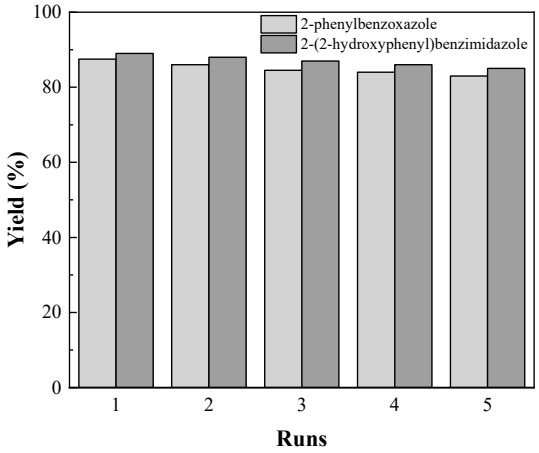

Figure 7. Recyclability of F,O,S-codoped g-C_3N_4 for the synthesis of 2-phenylbenzoxazole and 2-(2-hydroxyphenyl)benzimidazole.

2.2.2. Spectral Data of the Synthesized Products

(2-Phenylbenzoxazole): ^{1}H NMR (500 MHz, $CDCl_3$) δ 8.66 (s, 1H), 7.96–7.88 (m, 2H), 7.58–7.46 (m, 3H), 7.31 (dd, *J* = 7.9, 1.5 Hz, 1H), 7.29–7.23 (m, 1H), 7.12 (dd, *J* = 8.1, 1.4 Hz, 1H), 6.96 (td, *J* = 7.6, 1.4 Hz, 1H); ^{13}C NMR (125 MHz) δ 162.60, 150.72, 140.62, 131.49, 129.08, 128.98, 127.55, 125.53, 125.22, 120.07, 111.09. ATR-FTIR: 1624, 1574, 1481 (C=C), 1450, 1380, 1313, 1279, 1249, 1199, 1147, 763, 688, 637 cm^{-1}.

2-(4-Chlorophenyl)-1,3-benzoxazole: ^{1}H NMR (500 MHz, $CDCl_3$) δ 7.91–7.85 (m, 2H), 7.64–7.54 (m, 2H), 7.46–7.37 (m, 3H); ^{13}C NMR (125 MHz) δ 162.31, 150.76, 140.81, 136.93, 129.28, 129.12, 128.42, 125.53, 125.22, 120.07, 111.09. ATR-FTIR: 1625, 1585, 1567, 1480, 1380, 1237, 1196, 1170, 1146, 1094, 820, 791, 751, 669 cm^{-1}.

2-(2-Napthyl)-1,3-benzoxazole: ^{1}H NMR (500 MHz, $CDCl_3$) δ 8.81 (t, *J* = 3.0 Hz, 1H), 8.19–8.13 (m, 2H), 8.02–7.86 (m, 3H), 7.62–7.52 (m, 2H), 7.40–7.28 (m, 1H), 7.24 (ddt, *J* = 8.7, 7.3, 1.2 Hz, 1H), 7.08 (dq, *J* = 8.1, 1.3 Hz, 1H), 6.95 (td, *J* = 7.6, 1.4 Hz, 1H); ^{13}C NMR (125 MHz) δ 163.87, 150.58, 140.46, 134.84, 133.59, 128.91, 127.95, 127.90, 127.22, 126.96, 126.86, 126.42, 126.02, 125.53, 125.22, 120.08, 111.07. ATR-FTIR: 1625, 1585, 1480, 1380, 1275, 1239, 1196, 1170, 1146, 1094, 821, 791, 751, 669 cm^{-1}.

2(-2-Hydroxyphenyl)-1,3-benzoxazole: ^{1}H NMR (500 MHz, $CDCl_3$) δ 8.61 (s, 1H), 7.86–7.77 (m, 2H), 7.27 (d, *J* = 7.1 Hz, 1H), 7.17 (ddd, *J* = 7.9, 7.3, 1.5 Hz, 1H), 7.03–6.87 (m, 3H), 6.87–6.66 (m, 1H), 1.25 (s, 1H); ^{13}C NMR (125 MHz) δ 162.88, 158.71, 149.19, 139.44, 133.84, 127.24, 125.51, 125.38, 119.77, 119.73, 117.24, 111.69, 110.75. ATR-FTIR: 1631, 1590, 1544, 1486, 1454, 1407, 1238, 1192, 1050, 941, 892, 840, 796, 741, 706 cm^{-1}.

2-(2-Methoxyphenyl)-1,3-benzoxazole: ^{1}H NMR (500 MHz, $CDCl_3$) δ 9.23 (s, 1H), 9.20 (s, 1H), 8.46 (dd, *J* = 7.7, 1.8 Hz, 1H), 7.65 (ddd, *J* = 8.8, 7.2, 1.8 Hz, 1H), 7.35–7.19 (m, 4H), 7.15 (dd, *J* = 8.1, 1.4 Hz, 1H), 7.03 (td, *J* = 7.5, 1.4 Hz, 1H), 4.04 (s, 3H), 3.87–3.83 (m, 2H); ^{13}C NMR (125 MHz) δ 189.55, 161.94, 159.60, 154.85, 151.49, 144.58, 139.10, 136.89, 136.79, 133.34, 128.15, 127.86, 127.62, 124.66, 124.60, 120.97, 120.06, 119.62, 117.14, 116.42, 115.09, 114.93, 112.90, 112.11, 56.17, 56.06, 40.33, 40.16, 40.00, 39.83, 39.66, 39.50, 39.33. ATR-FTIR: 1615, 1586, 1503, 1485, 1455, 1430, 1370, 1290, 1237, 1208, 1020, 897, 763, 749 cm^{-1}.

2-Phenylbenzimidazole: ^{1}H NMR (500 MHz, $CDCl_3$) δ 8.35–8.29 (m, 2H), 7.68–7.59 (m, 2H), 7.56–7.45 (m, 4H), 7.32–7.23 (m, 2H); ^{13}C NMR (125 MHz) δ 152.01, 140.54, 139.44, 130.31, 130.29, 129.04, 127.70, 123.26, 123.11, 117.88, 115.08. ATR-FTIR: 3060, 1603, 1493, 1470, 1449, 1441, 1392, 1360, 1331, 1277, 1249, 1178, 1165, 1029, 1002, 990, 972, 930, 822, 775, 764, 741, 733, 697 cm^{-1}.

2-(4-Chlorophenyl)benzimidazole: ^{1}H NMR (500 MHz, $CDCl_3$) δ 7.93–7.87 (m, 1H), 7.68–7.59 (m, 1H), 7.52–7.46 (m, 1H), 7.31–7.23 (m, 1H);. ^{13}C NMR (125 MHz) δ 154.49, 140.55, 139.44, 136.25, 130.28, 128.93, 127.92, 123.26, 123.11, 117.88, 115.08. ATR-FTIR: 1602, 1587, 1489, 1471, 1447, 1428, 1397, 1372, 1320, 1273, 1226, 1120, 1107, 1089, 1016, 963, 923, 902, 875, 829, 765, 742, 728 cm^{-1}.

2-(2-Naphthylmethyl)benzimidazole: ^{1}H NMR (500 MHz, $CDCl_3$) δ 8.69 (s, 1H), 8.24–8.14 (m, 3H), 8.03–7.79 (m, 5H), 7.81–7.69 (m, 1H), 7.72–7.62 (m, 1H), 7.62–7.36 (m, 4H), 7.36–7.22 (m, 1H), 7.13 (ddd, *J* = 14.9, 7.4, 1.4 Hz, 2H), 6.86⁻6.79 (m, 2H), 6.79–6.68 (m, 1H), 4.39 (s, 4H); ^{13}C NMR (125 MHz) δ 153.31, 142.13, 139.05, 134.56, 132.96, 128.72, 128.69, 127.90, 127.11, 127.10, 126.99, 126.42, 124.34, 123.26, 123.11, 117.82, 115.24. ATR-FTIR: 3475, 3376, 1615, 1601, 1496, 1457, 1323, 1306, 1278, 1240, 1203, 1173, 1121, 977, 966, 859, 821, 767, 745 cm^{-1}.

2-(2-Hydroxyphenyl)benzimidazole: ^{1}H NMR (500 MHz, $CDCl_3$) δ 7.83 (dd, *J* = 10.2, 1.2 Hz, 1H), 7.64–7.54 (m, 2H), 7.46–7.37 (m, 2H), 7.28–7.21 (m, 1H), 7.08 (ddd, *J* = 10.1, 7.7, 1.4 Hz, 1H), 6.94 (dd, *J* = 8.3, 1.4 Hz, 1H); ^{13}C NMR (125 MHz) δ 162.88, 158.71, 149.19, 139.44, 133.84, 127.24, 125.51, 125.38, 119.77, 119.73, 117.24, 111.69, 110.75. ATR-FTIR: 3308 (OH, NH), 1610 (C=N) cm^{-1}.

2-(2-Methoxyphenyl)benzimidazole: ^{1}H NMR (500 MHz, $CDCl_3$) δ 7.98 (dd, *J* = 8.4, 1.3 Hz, 1H), 7.67–7.58 (m, 2H), 7.34–7.23 (m, 2H), 7.17 (ddd, *J* = 8.6, 7.5, 1.2 Hz, 1H), 6.98 (dd, *J* = 7.7, 1.2 Hz, 1H), 3.89 (s, 2H); ^{13}C NMR (125 MHz) δ 158.13, 151.33, 138.62, 137.57, 131.41, 131.10, 123.24, 123.11, 120.97, 117.01, 114.98, 114.34, 111.60, 55.80. ATR-FTIR: 3475,

3375, 1615 (C=N), 1601, 1496, 1457, 1323, 1306, 1240 (C–O), 1203, 1173, 1141, 1122, 977, 965, 900, 872, 859, 821, 767, 745 cm^{-1}.

3. Discussion

3.1. On the Role of the Doping Elements

The doping heteroatoms would be involved in the modification of the inter-layer spacing (an effective way to promote the migration of photogenerated electrons between the g-C_3N_4 structural units) and would provide more active sites. According to Li et al. [28], –NH– and –C=O/C–O active functional groups, N defects, and heteroatom-dopants can act as active sites in g-C_3N_4 photocatalysts. However, conventional g-C_3N_4 has few reactive sites and adsorption sites due to its stacked bulk structure and stable π-conjugated system. Heteroatom doping can increase the adsorption activity sites of g-C_3N_4 to specifically adsorb some reaction substrates. Moreover, according to Katsumata et al. [29], some of the incorporated dopants (such as P and S) can promote visible light absorption and the separation of charge carriers.

The modifications would be a result of the radius of doping atoms being larger than those of C and N ones. Among the doping atoms, S would be the one that, after P, is the most capable of boosting the catalytic activity of g-C_3N_4: it has a higher covalent radius (105 pm) than those of C (76 pm) and N (71 pm) and has an electronegativity close to that of C (2.55). According to Li, Li, Zhang, Fan and Xiang [28], heteroatom doping promotes the migration of photogenerated electrons between structural units, in such a way that the active surface sites (associated with the active functional groups introduced) can have sufficient photogenerated carriers to participate in photocatalysis.

Although according to Stolbov and Zuluaga [30], S-doping makes g-C_3N_4 a conductor, which is a very unfavorable transformation for a photocatalyst, the co-doping with other heteroatoms enhances the photocatalytic activity of pristine g-C_3N_4. Thus, it has been reported that, in a P,S,O-codoped g-C_3N_4 catalyst, the P and S dopants were integrated into C or N sites to fill intrinsic vacancies, increasing free electrons, raising the Fermi level, and leading to an enhanced photocatalytic activity for methylene blue degradation [13]. In this paper, instead of P-doping, the effect of F-doping was assayed, given that the introduction of F atoms into the g-C_3N_4 framework has been reported to improve charge separation because of the affected π band and long-pair electron states [22]. In the same line, Wang et al. [31] and Liu et al. [32] noted that fluorination would entail lower charge transfer rates, but the charge separation ability would be much higher than that of pristine g-C_3N_4, resulting in enhanced photocatalytic activity of the modified samples.

3.2. Reaction Mechanism

Under visible light irradiation, F,O,S-doped g-C_3N_4 absorbs photons, and electron-hole pairs are generated. The photogenerated holes (h^+) in the valence band of the catalyst would not have the ability to oxidize water to hydroxyl radicals (•OH) (because the oxidation potential would not be sufficient for the oxidation of H_2O), but the photogenerated electrons (e^-) in the conduction band of F,O,S-codoped g-C_3N_4 would be able to reduce the molecular oxygen to form reactive superoxide radical ions ($\bullet O^{2-}$) [33]. Based on this feature, a tentative reaction pathway for the formation of benzoxazoles/benzimidazoles is presented in Figure 8, analogous to the one proposed by Li et al. [34]. First, the condensation of 2-aminophenol/2-phenylenediamine with the aldehyde would take place to form a Schiff base, which would transform into the intermediary benzoxazoline/benzimidazoline; the highly reactive $\bullet O_2^-$ radicals would then be the actual oxidants for the oxidative cyclo-dehydrogenation of the intermediate to afford the final product (benzoxazole/benzimidazole).

This predominance of $\bullet O^{2-}$ radicals (with a negligible intervention of •OH radicals) would contribute to the preservation of the stability of the F,O,S-doped g-C_3N_4 photocatalyst: as noted by Xiao et al. [35], the mediation of these radicals does not introduce any instability for a g-C_3N_4 type catalyst.

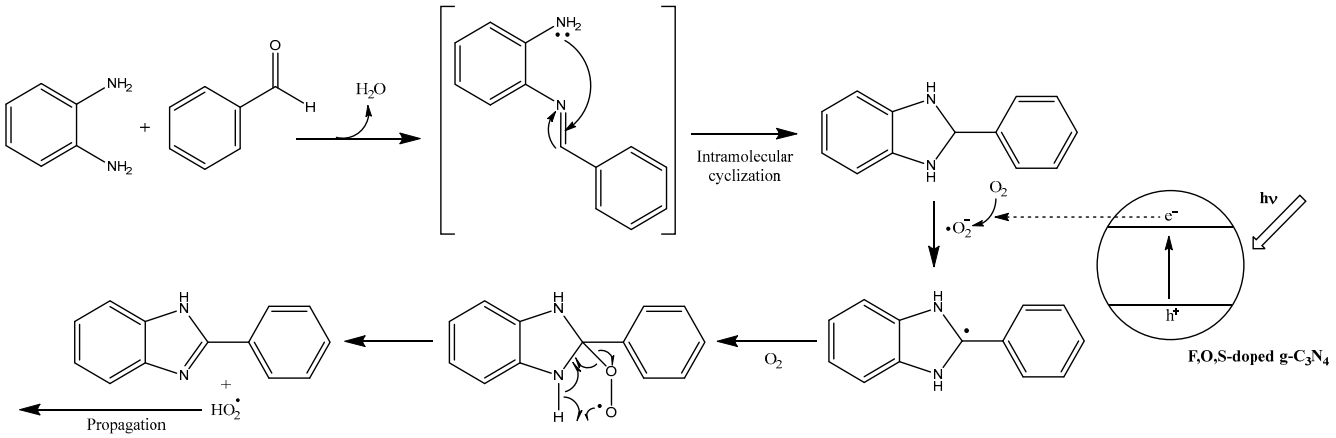

Figure 8. A possible reaction pathway for the formation of benzimidazole.

3.3. On the Advantages of the Novel Photocatalyst for the Synthesis of Benzoxazoles and Benzimidazoles

To the best of the authors' knowledge, one of the best catalytic systems currently available for the synthesis of 2-arylbezoxazoles is $NiFe_2O_4$@SiO_2@aminoglucose [36], which has been reported to catalyze the reaction at room temperature in 10 min under solvent-free conditions. However, it has the disadvantages of being a multistep synthesis and requiring a high catalyst load (50 mg/mmoL). In this regard, the catalyst proposed herein would also operate at room temperature (30 °C), would have comparable reusability, and a lower load of catalyst would be required.

Another excellent catalyst for the synthesis of benzoxazoles would be mesoporous titania-alumina mixed oxide in combination with titanium tetraisopropoxide (as Lewis acid) and 30% H_2O_2 (as an oxidant), reported by Bahrami and Karami [37], which reached a 94% yield. In comparison, the proposed F,O,S-codoped g-C_3N_4 photocatalyst obtains slightly lower yields, but does not require any oxidant and is not sensitive to air and moisture.

4. Materials and Methods

4.1. Reagents

Melamine cyanurate (CAS 37640-57-6) was supplied by Nachmann S.r.l. (Milano, MI, USA). Trifluoromethanesulfonic acid (CAS 1493-13-6), 2-aminophenol (CAS 95-55-6), 1,2-phenylenediamine (CAS 95-54-5), benzaldehyde (CAS 100-52-7), 4-chlorobenzaldehyde (CAS 104-88-1), 2-naphthaldehyde (CAS 66-99-9), 2-hydroxybenzaldehyde (CAS 90-02-8), and 2-methoxybenzaldehyde (CAS 135-02-4) were purchased from Sigma Aldrich Química (Madrid, Spain) and used without further purification.

4.2. Synthesis of the Photocatalyst

F,O,S-codoped graphitic carbon nitride catalyst was prepared using melamine cyanurate ($C_3H_6N_6 \cdot C_3H_3N_3O_3$) soaked in trifluoromethanesulfonic acid (CF_3SO_3H), followed by heating at 550 °C for 50 min in a ceramic crucible in a convective tubular oven GVA 12/900, power: 5.460 kW, heating length: 900 mm, Tmax: 1200 °C (Carbolite, Sheffield, UK). In the thermal treatment process, ca. 90% of CF_3SO_3H decomposed, releasing CO and SO_2.

4.3. Characterization of the Photocatalyst

Scanning electron microscopy images were taken using a QUANTA 200 FEG ESEM (FEI, Hillsboro, OR, USA).

Transmission electron microscopy micrographs were obtained with a JEM–FS2200 HRP system (JEOL Ltd., Akishima, Tokyo, Japan) at 200 kV.

The infrared spectra were registered using a Nicolet iS50 (Thermo Scientific, Waltham, MA, USA) Fourier-transform infrared (FTIR) spectrometer, equipped with an in-built

diamond attenuated total reflectance system (ATR). The spectra were collected over the 400–4000 cm^{-1} range, with a 1 cm^{-1} spectral resolution.

The phase composition of the samples was analyzed using a D8 Advance (Bruker, Billerica, MA, USA) diffractometer equipped with Cu Kα (λ = 0.15406 nm) X-ray source. The X-ray powder diffraction pattern was recorded in the 2θ = 5–70° range.

The CHNS elemental analysis was carried out using a Leco CHNS-932 analyzer.

Fluorine content was determined by total combustion-ion chromatography using a 930 Compact IC Flex Oven/SeS/PP/Deg ionic chromatograph (Metrohm, Herisau, Switzerland), with an MMS 5000 Analytik Jena combustion module with autosampler and a 920 Metrohm absorber module.

Surface chemical composition was analyzed through X-ray photoelectron spectroscopy with an AXIS Supra (Kratos Analytical, Manchester, UK) spectrometer using mono Al Kα radiation at a power of 120 W (8 mA/15 kV). Spectra were acquired at 10^{-8} torr. Spectra were measured using the hybrid-slot lens mode, covering an area of approximately 700 × 300 μm. Spectra have been charge-corrected to the adventitious carbon C1s (c-C) line set to 284.5 eV and analyzed using CasaXPS software (version 2.3.15).

Energy-dispersive X-ray spectroscopy analyses were conducted with an EDAX Genesis module coupled to the ESEM.

The absorption spectra were recorded using an RP20 high-OH reflection probe, a SLS204 stabilized deuterium lamp, and a CCS200/M CCD spectrometer, all three supplied by Thorlabs (Newton, NJ, USA). Emission spectra were measured with the same spectrometer using a 365 nm LED source. An FGUV11 275–375 nm UV bandpass filter and a FEL400 longpass filter with 400 nm cut-on wavelength, both from Thorlabs, were used for the excitation and the emission, respectively.

4.4. Synthesis of Benzoxazoles and Benzimidazoles

In a typical photocatalytic reaction of benzoxazoles and benzimidazoles, a mixture of 2-aminophenol or 2-phenylenediamine (1 mmoL), a benzaldehyde (either benzaldehyde, 4-chlorobenzaldehyde, 2-naphthaldehyde, 2-hydroxybenzaldehyde, 2-methoxybenzalde hyde; 1 mmol), and F,O,S-doped g-C_3N_4 catalyst (at concentrations ranging from 0.3 to 3 wt%), were taken into a round-bottom flask using methanol as a solvent and stirred at room temperature. The catalyst was dispersed by ultrasonication for 5 min in the dark, in periods of 1 min so that the temperature did not exceed 40 °C. After irradiation with a 300 W Xe lamp for 15–30 min at 30 °C under vigorous stirring and completion of the reaction (monitored by thin-layer chromatography, TLC), the reaction mixture was poured into ice-cold water and the catalyst was separated by centrifugation and purified by washing with acetone for reuse. The organic layer was purified by column chromatography over silica gel (using ethyl acetate/petroleum ether as eluent) and concentrated under reduced pressure.

The reaction of 2-amino phenol with the above-cited benzaldehydes (Figure 9a) results in the 2-arylbenzoxazoles shown in Figure 6a. In turn, a scheme of the reaction of 2-phenylenediamine with the same benzaldehydes is presented in Figure 9b, and the resulting products are shown in Figure 6b.

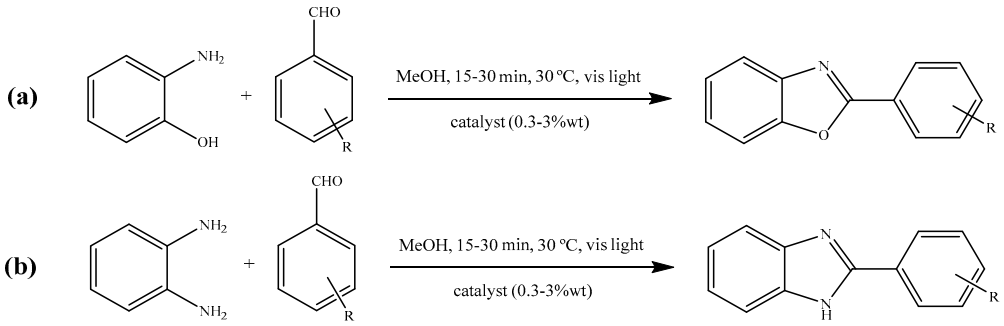

Figure 9. (**a**) Synthesis of 2-arylbenzoxazoles; (**b**) synthesis of 2-arylbenzimidazoles.

The synthesized 2-arylbenzoxazoles and 2-arylbenzimidazoles were characterized by proton and carbon-13 nuclear magnetic resonance (^{1}H-NMR and ^{13}C-NMR, respectively) at the Laboratorio de Técnicas Instrumentales at Universidad de Valladolid (Valladolid, Spain) using an RMN 500 (Agilent Technologies, Santa Clara, CA, USA), in deuterochloroform (^{1}H-NMR) or dimethyl sulfoxide-d_6 (^{13}C-NMR). Their vibrational characterization was conducted using the same ATR-FTIR equipment described in the photocatalyst characterization subsection. For selectivity determinations, high-resolution mass spectra (HRMS) were recorded on an Agilent 5973 (Agilent Technologies) mass spectrometer with a time-of-flight (TOF) mass analyzer using the ESI technique.

5. Conclusions

An alternative photocatalyst for the synthesis of both 2-benzodioxazoles and 2-aylbenzimidazoles via condensation–aromatization of 2-aminophenol or 2-phenylenediamine with suitable aldehydes (viz. benzaldehyde, 4-chlorobenzaldehyde, 2-naphthaldehyde, 2-hydroxybenzaldehyde, and 2-methoxybenzaldehyde) was synthesized and characterized by SEM, TEM, ATR-FTIR, XRPD, XPS, EDS, and UV-Vis techniques. XPS data confirmed the doping of g-C_3N_4 with F (ca. 9%at.), O (ca. 9%at.), and S (ca. 2%at.). For F,O,S-codoped g-C_3N_4 photocatalyst contents in the 1–2.3 wt% range, yields in the 75.2–87.5% and 75.0–89% intervals were obtained for benzoxazoles and benzimidazoles, respectively, at a low temperature (30 °C), in short times (15-30 min), with good catalyst reusability and selectivities above 88%. The reported findings suggest that F,O,S-codoped g-C_3N_4 would have comparable performance to that of metal-based catalysts, with advantages in terms of lower catalyst load and lower process temperature requirements.

Supplementary Materials: The following supporting information can be downloaded at: https://www.mdpi.com/article/10.3390/catal13020385/s1, Figure S1: ATR-FTIR spectrum of F,O,S-codoped g-C_3N_4; Figure S2: X-ray powder diffraction pattern of F,O,S-codoped g-C_3N_4; Figure S3: EDS analysis of F,O,S-codoped g-C_3N_4; Figure S4: EDS analysis of F,O,S-codoped g-C_3N_4: elemental mapping; Figure S5: Comparison of the luminescence spectrum of F,O,S-codoped g-C_3N_4 and pristine g-C_3N_4; Figure S6: Intermediate and desired products considered in the selectivity evaluation; Figure S7: ATR-FTIR spectra of the F,O,S-codoped g-C_3N_4 photocatalyst before 1st use and after 5 runs; Table S1: CHNS elemental analysis results of F,O,S-codoped g-C_3N_4.

Author Contributions: Conceptualization, J.M.-G.; methodology, J.M.-G. and P.M.-R.; validation, C.A.-J.; formal analysis, A.S.-A., P.C.-P., G.A., J.M.-G. and P.M.-R.; investigation, A.S.-A., E.S.-H., C.A.-J., P.C.-P., G.A., J.M.-G. and P.M.-R.; resources, C.A.-J. and J.M.-G.; writing—original draft preparation, A.S.-A., E.S.-H., P.C.-P., G.A., J.M.-G. and P.M.-R.; writing—review and editing, J.M.-G. and P.M.-R.; visualization, P.C.-P., G.A. and P.M.-R.; supervision, P.M.-R. All authors have read and agreed to the published version of the manuscript.

Funding: This research was partly funded by Junta de Castilla y León through the grants to support recognized research groups awarded to GIR-TADRUS research group.

Institutional Review Board Statement: Not applicable.

Informed Consent Statement: Not applicable.

Data Availability Statement: The data presented in this study are available on request from the corresponding author. The data are not publicly available due to their relevance to an ongoing Ph.D. thesis.

Acknowledgments: To the Parque Científico and the Laboratorio de Técnicas Instrumentales of the Universidad de Valladolid, for conducting the characterization.

Conflicts of Interest: The authors declare no conflict of interest.

References

1. Seth, K.; Garg, S.K.; Kumar, R.; Purohit, P.; Meena, V.S.; Goyal, R.; Banerjee, U.C.; Chakraborti, A.K. 2-(2-arylphenyl)benzoxazole as a novel anti-inflammatory scaffold: Synthesis and biological evaluation. *ACS Med. Chem. Lett.* **2014**, *5*, 512–516. [CrossRef] [PubMed]
2. Zhang, W.; Liu, J.; Macho, J.M.; Jiang, X.; Xie, D.; Jiang, F.; Liu, W.; Fu, L. Design, synthesis and antimicrobial evaluation of novel benzoxazole derivatives. *Eur. J. Med. Chem.* **2017**, *126*, 7–14. [CrossRef] [PubMed]
3. Mortimer, C.G.; Wells, G.; Crochard, J.-P.; Stone, E.L.; Bradshaw, T.D.; Stevens, M.F.G.; Westwell, A.D. Antitumor benzothiazoles. 26. 2-(3,4-dimethoxyphenyl)-5-fluorobenzothiazole (GW 610, NSC 721648), a simple fluorinated 2-arylbenzothiazole, shows potent and selective inhibitory activity against lung, colon, and breast cancer cell lines. *J. Med. Chem.* **2005**, *49*, 179–185. [CrossRef] [PubMed]
4. Gerova, M.S.; Stateva, S.R.; Radonova, E.M.; Kalenderska, R.B.; Rusew, R.I.; Nikolova, R.P.; Chanev, C.D.; Shivachev, B.L.; Apostolova, M.D.; Petrov, O.I. Combretastatin A-4 analogues with benzoxazolone scaffold: Synthesis, structure and biological activity. *Eur. J. Med. Chem.* **2016**, *120*, 121–133. [CrossRef]
5. Nguyen, T.T.; Nguyen, X.-T.T.; Nguyen, T.-L.H.; Tran, P.H. Synthesis of benzoxazoles, benzimidazoles, and benzothiazoles using a brønsted acidic ionic liquid gel as an efficient heterogeneous catalyst under a solvent-free condition. *ACS Omega* **2019**, *4*, 368–373. [CrossRef]
6. Vafaeezadeh, M.; Alinezhad, H. Brønsted acidic ionic liquids: Green catalysts for essential organic reactions. *J. Mol. Liq.* **2016**, *218*, 95–105. [CrossRef]
7. Pham, P.T.; Nguyen, H.T.; Nguyen, T.T.; Nguyen, L.H.T.; Dang, M.-H.D.; Doan, T.L.H.; Pham, D.D.; Nguyen, C.T.; Tran, P.H. Rapid and simple microwave-assisted synthesis of benzoxazoles catalyzed by [cholineCl][oxalic acid]. *Catalysts* **2022**, *12*, 1394. [CrossRef]
8. Verma, S.K.; Verma, R.; Girish, Y.R.; Xue, F.; Yan, L.; Verma, S.; Singh, M.; Vaishnav, Y.; Shaik, A.B.; Bhandare, R.R.; et al. Heterogeneous graphitic carbon nitrides in visible-light-initiated organic transformations. *Green Chem.* **2022**, *24*, 438–479. [CrossRef]
9. Wang, J.; Wang, S. A critical review on graphitic carbon nitride ($g\text{-}C_3N_4$)-based materials: Preparation, modification and environmental application. *Coord. Chem. Rev.* **2022**, *453*, 214338. [CrossRef]
10. Zhang, L.; Liu, D.; Guan, J.; Chen, X.; Guo, X.; Zhao, F.; Hou, T.; Mu, X. Metal-free $g\text{-}C_3N_4$ photocatalyst by sulfuric acid activation for selective aerobic oxidation of benzyl alcohol under visible light. *Mater. Res. Bull.* **2014**, *59*, 84–92. [CrossRef]
11. Goodarzi, N.; Rashidizadeh, A.; Ghafuri, H. $ompg\text{-}C_3N_4/SO_3H$ organocatalyst-mediated green synthesis of 1,2-dihydro-1-arylnaphtho[1,2-e][1,3] oxazin-3-ones under solvent-free and mild conditions: A fast and facile one-pot three-component approach. *Mon. Chem.—Chem. Mon.* **2020**, *151*, 791–798. [CrossRef]
12. Veisi, H.; Mohammadi, P.; Ozturk, T. Design, synthesis, characterization, and catalytic properties of $g\text{-}C_3N_4\text{-}SO_3H$ as an efficient nanosheet ionic liquid for one-pot synthesis of pyrazolo[3,4-b]pyridines and bis(indolyl)methanes. *J. Mol. Liq.* **2020**, *303*, 112625. [CrossRef]
13. Chu, Y.-C.; Lin, T.-J.; Lin, Y.-R.; Chiu, W.-L.; Nguyen, B.-S.; Hu, C. Influence of P,S,O-Doping on $g\text{-}C_3N_4$ for hydrogel formation and photocatalysis: An experimental and theoretical study. *Carbon* **2020**, *169*, 338–348. [CrossRef]
14. Dante, R.C.; Martín-Ramos, P.; Sánchez-Arévalo, F.M.; Huerta, L.; Bizarro, M.; Navas-Gracia, L.M.; Martín-Gil, J. Synthesis of crumpled nanosheets of polymeric carbon nitride from melamine cyanurate. *J. Solid State Chem.* **2013**, *201*, 153–163. [CrossRef]
15. Jiang, J.; Zou, J.; Wee, A.T.S.; Zhang, W. Use of single-layer $g\text{-}C_3N_4/Ag$ hybrids for surface-enhanced raman scattering (SERS). *Sci. Rep.* **2016**, *6*, 34599. [CrossRef]
16. Phuc, N.V.; An, D.T.; Tri, N.N.; Ha, T.H.; Hien, T.T.T.; Hung, N.P.; Vo, V. Synthesis and photocatalytic activity of fluorine doped-$g\text{-}C_3N_4$. *Appl. Mech. Mater.* **2019**, *889*, 24–32. [CrossRef]
17. Mazánek, V.; Jankovský, O.; Luxa, J.; Sedmidubský, D.; Janoušek, Z.; Šembera, F.; Mikulics, M.; Sofer, Z. Tuning of fluorine content in graphene: Towards large-scale production of stoichiometric fluorographene. *Nanoscale* **2015**, *7*, 13646–13655. [CrossRef]
18. You, R.; Dou, H.; Chen, L.; Zheng, S.; Zhang, Y. Graphitic carbon nitride with S and O codoping for enhanced visible light photocatalytic performance. *RSC Adv.* **2017**, *7*, 15842–15850. [CrossRef]
19. Wang, X.; Wang, W.; Liu, Y.; Ren, M.; Xiao, H.; Liu, X. Characterization of conformation and locations of C–F bonds in graphene derivative by polarized ATR-FTIR. *Anal. Chem.* **2016**, *88*, 3926–3934. [CrossRef]
20. Lin, W.; Lu, K.; Zhou, S.; Wang, J.; Mu, F.; Wang, Y.; Wu, Y.; Kong, Y. Defects remodeling of $g\text{-}C_3N_4$ nanosheets by fluorine-containing solvothermal treatment to enhance their photocatalytic activities. *Appl. Surf. Sci.* **2019**, *474*, 194–202. [CrossRef]
21. Yang, X.; Qian, F.; Zou, G.; Li, M.; Lu, J.; Li, Y.; Bao, M. Facile fabrication of acidified $g\text{-}C_3N_4/g\text{-}C_3N_4$ hybrids with enhanced photocatalysis performance under visible light irradiation. *Appl. Catal. B Environ.* **2016**, *193*, 22–35. [CrossRef]
22. Sun, L.; Li, Y.; Feng, W. Gas-phase fluorination of $g\text{-}C_3N_4$ for enhanced photocatalytic hydrogen evolution. *Nanomaterials* **2021**, *12*, 37. [CrossRef] [PubMed]
23. Liu, G.; Niu, P.; Sun, C.; Smith, S.C.; Chen, Z.; Lu, G.Q.; Cheng, H.-M. Unique electronic structure induced high photoreactivity of sulfur-doped graphitic C_3N_4. *J. Am. Chem. Soc.* **2010**, *132*, 11642–11648. [CrossRef] [PubMed]
24. Wang, Y.; Di, Y.; Antonietti, M.; Li, H.; Chen, X.; Wang, X. Excellent visible-light photocatalysis of fluorinated polymeric carbon nitride solids. *Chem. Mater.* **2010**, *22*, 5119–5121. [CrossRef]

25. Dong, G.; Zhao, K.; Zhang, L. Carbon self-doping induced high electronic conductivity and photoreactivity of g-C_3N_4. *Chem. Commun.* **2012**, *48*, 6178. [CrossRef]
26. Cheng, H.; Feng, Y.; Fu, Y.; Zheng, Y.; Shao, Y.; Bai, Y. Understanding and minimizing non-radiative recombination losses in perovskite light-emitting diodes. *J. Mater. Chem. C* **2022**, *10*, 13590–13610. [CrossRef]
27. Layek, S.; Agrahari, B.; Kumar, A.; Dege, N.; Pathak, D.D. Synthesis and X-ray crystal structures of three new nickel(II) complexes of benzoylhydrazones: Catalytic applications in the synthesis of 2-arylbenzoxazoles. *Inorg. Chim. Acta* **2019**, *500*, 119222. [CrossRef]
28. Li, Y.; Li, X.; Zhang, H.; Fan, J.; Xiang, Q. Design and application of active sites in g-C_3N_4-based photocatalysts. *J. Mater. Sci. Technol.* **2020**, *56*, 69–88. [CrossRef]
29. Katsumata, H.; Tateishi, I.; Furukawa, M.; Kaneco, S. Highly photocatalytic hydrogen generation over P-doped g-C_3N_4 with aromatic ring structure. *Mater. Lett.* **2021**, *299*, 130068. [CrossRef]
30. Stolbov, S.; Zuluaga, S. Sulfur doping effects on the electronic and geometric structures of graphitic carbon nitride photocatalyst: Insights from first principles. *J. Phys. Condens. Matter* **2013**, *25*, 085507. [CrossRef]
31. Wang, H.; Zhang, X.; Xie, J.; Zhang, J.; Ma, P.; Pan, B.; Xie, Y. Structural distortion in graphitic-C_3N_4 realizing an efficient photoreactivity. *Nanoscale* **2015**, *7*, 5152–5156. [CrossRef]
32. Liu, H.; Wang, X.; Xu, H.; Luo, C. Facile synthesis of F-doped g-C_3N_4/$Bi_2Fe_4O_9$ heterostructure with Z-scheme for enhanced photocatalytic performance in NO oxidation. *J. Phys. Chem. Solids* **2020**, *146*, 109500. [CrossRef]
33. Kobkeatthawin, T.; Trakulmututa, J.; Amornsakchai, T.; Kajitvichyanukul, P.; Smith, S.M. Identification of active species in photodegradation of aqueous imidacloprid over g-C_3N_4/TiO_2 nanocomposites. *Catalysts* **2022**, *12*, 120. [CrossRef]
34. Li, Z.; Song, H.; Guo, R.; Zuo, M.; Hou, C.; Sun, S.; He, X.; Sun, Z.; Chu, W. Visible-light-induced condensation cyclization to synthesize benzimidazoles using fluorescein as a photocatalyst. *Green Chem.* **2019**, *21*, 3602–3605. [CrossRef]
35. Xiao, J.; Xie, Y.; Rabeah, J.; Brückner, A.; Cao, H. Visible-light photocatalytic ozonation using graphitic C_3N_4 catalysts: A hydroxyl radical manufacturer for wastewater treatment. *Acc. Chem. Res.* **2020**, *53*, 1024–1033. [CrossRef]
36. Fekri, L.Z.; Nikpassand, M.; Shariati, S.; Aghazadeh, B.; Zarkeshvari, R.; Norouz pour, N. Synthesis and characterization of amino glucose-functionalized silica-coated $NiFe_2O_4$ nanoparticles: A heterogeneous, new and magnetically separable catalyst for the solvent-free synthesis of 2,4,5–trisubstituted imidazoles, benzo[d]imidazoles, benzo[d] oxazoles and azo-linked benzo[d]oxazoles. *J. Organomet. Chem.* **2018**, *871*, 60–73. [CrossRef]
37. Bahrami, K.; Karami, Z. Core/shell structured ZnO@SiO_2-TTIP composite nanoparticles as an effective catalyst for the synthesis of 2-substituted benzimidazoles and benzothiazoles. *J. Exp. Nanosci.* **2018**, *13*, 272–283. [CrossRef]